Journal of Geophysical Research: Solid Earth

RESEARCH ARTICLE
10.1029/2018JB015790

Melting Phase Relations and Element Partitioning in MORB to Lowermost Mantle Conditions

Shigehiko Tateno[1], Kei Hirose[1,2], Shuhei Sakata[3,4], Kyoko Yonemitsu[1], Haruka Ozawa[1,5,6], Takafumi Hirata[3,7], Naohisa Hirao[8], and Yasuo Ohishi[8]

[1]Earth-Life Science Institute, Tokyo Institute of Technology, Meguro, Japan, [2]Department of Earth and Planetary Science, The University of Tokyo, Bunkyo, Japan, [3]Laboratory for Planetary Sciences, Division of Earth and Planetary Sciences, Kyoto University, Kyoto, Japan, [4]Now at Department of Chemistry, Faculty of Science, Gakushuin University, Mejiro, Japan, [5]Laboratory of Ocean–Earth Life Evolution Research, Japan Agency for Marine–Earth Science and Technology, Yokosuka, Japan, [6]Now at Nuclear Science and Engineering Center, Japan Atomic Energy Agency, Tokai-mura, Japan, [7]Now at Geochemical Research Center, The University of Tokyo, Bunkyo, Japan, [8]Japan Synchrotron Radiation Research Institute, Sayo-cho, Japan

Key Points:
- Melting relations and element partitioning in MORB have been studied comprehensively by EPMA, TEM, LA-ICP-MS, and XRD to the CMB pressure
- Iron-rich partial melts form from MORB materials at the base of the mantle, whose liquidus phase is Ca-perovskite
- Strong pressure effect on Ca-pv/melt element partitioning due to higher compressibility of large cations compared to a crystal lattice site

Correspondence to:
S. Tateno,
tateno@elsi.jp

Citation:
Tateno, S., Hirose, K., Sakata, S., Yonemitsu, K., Ozawa, H., Hirata, T., et al. (2018). Melting phase relations and element partitioning in MORB to lowermost mantle conditions. *Journal of Geophysical Research: Solid Earth*, *123*. https://doi.org/10.1029/2018JB015790

Received 18 MAR 2018
Accepted 18 JUN 2018
Accepted article online 26 JUN 2018

Abstract Melting phase relations and crystal-melt element partitioning in a mid-oceanic ridge basalt bulk composition were studied to 135 GPa using laser-heated diamond-anvil cell techniques. Using field-emission-type electron microprobe (FE-EPMA), transmission electron microscope (TEM), and laser ablation-inductively-coupled plasma mass spectrometer (LA-ICP-MS), we obtained comprehensive analyses of major and trace elements in coexisting melt and solid phases. $CaSiO_3$-perovskite (Ca-pv) was found to be the liquidus phase throughout the lower mantle pressure range. Whereas silica, followed by Mg-perovskite, are the second and third crystallizing phases to pressures exceeding 100 GPa, postperovskite, closely followed by seifertite, succeed Ca-pv at 135 GPa. The partitioning of trace elements between Ca-pv and melts exhibited a strong pressure effect, possibly due to a combination of high compressibility of cations compared to the lattice site in Ca-pv and melt compressional effects. The Ca-pv/melt partition coefficients for Na and K (D_{Na} and D_K) increase with increasing pressure, with D_{Na} close to unity and D_K greater than unity at lowermost mantle pressures. Also, D_{Nd} becomes larger (or identical within uncertainty) than D_{Sm} in the deep lower mantle. Partial melt formed by 51% partial melting of mid-oceanic ridge basalt at 135 GPa showed marked iron-enrichment and should thus have negative buoyancy at the base of the mantle. The density of residual solid is almost identical to the PREM density, and therefore, it is likely to be involved in mantle convection and recycled to the surface.

1. Introduction

The subduction of mid-oceanic ridge basalt (MORB) crust introduces strong chemical heterogeneities in the mantle. Such material may have accumulated above the core-mantle boundary (CMB) since MORB materials are denser than surrounding mantle except at 660–720 km depth (e.g., Hirose et al., 2005; Irifune & Ringwood, 1993; Ono et al., 2001; Komiya, 2004; Ricolleau et al., 2010). MORB exhibits lower solidus temperature than pyrolite (Andrault, Pesce, et al., 2014; Hirose et al., 1999; Pradhan et al., 2015), and it has been argued that partial melting of MORB may be responsible for distinct seismic features known as ultralow-velocity zones where strong wave speed reduction is observed (Garnero & Helmberger, 1995; Lay et al., 2004). It is indeed compatible with localized observations of ultralow-velocity zones.

Melting phase relations of MORB have been studied by using a multianvil apparatus up to 27 GPa (Hirose & Fei, 2002; Yasuda et al., 1994). These studies reported that Ca-pv is the liquidus (first crystallizing) phase above 23 GPa and that partial melts are strongly enriched in FeO at uppermost lower mantle conditions. Also, Ca-pv/melt and $MgSiO_3$-rich perovskite (Mg-pv)/melt partition coefficients were determined for a variety of trace elements by using ion microprobe or laser ablation-inductively-coupled plasma mass spectrometer (LA-ICP-MS; Corgne et al., 2005; Hirose et al., 2004; Liebske et al., 2005). Yet little is known about partial melting of MORB materials at deeper levels, where diamond-anvil cell (DAC) techniques including compositional characterization of recovered samples are indispensable. Andrault, Pesce, et al. (2014) examined the melting of MORB to the CMB pressure to determine the melting temperature. They also reported that the first phase to disappear above solidus temperature changed from Mg-pv to a SiO_2 phase above ~70 GPa based on in situ X-ray diffraction (XRD) measurements. Detailed transmission electron microscope (TEM) analysis by Pradhan

et al. (2015), however, indicates that the crystallization sequence is Ca-pv, followed by silica, and finally by Mg-pv even at 101 GPa.

The crystal-melt partitioning of trace elements is of great importance for chemical differentiation upon partial melting. However, such trace element partitioning in the lower mantle has been examined only up to 27 GPa, and its pressure effect is still unknown. We carried out melting experiments on MORB compositions up to 135 GPa by laser-heated DAC experiments combined with textural/compositional characterization of recovered samples by fielde-mission-type electron microprobe (FE-EPMA), scanning TEM, and LA-ICP-MS. Melting sequence and major element compositions of coexisting melt and crystals are reported. We also show the pressure effect on the Ca-pv/melt element partitioning to 135 GPa. On the basis of these experimental results, we discuss dynamical and geochemical consequences of partial melting of MORB materials at the base of the mantle.

2. Experimental Techniques

2.1. Melting Experiments at High Pressure

We used a couple of glass starting materials. One is anhydrous glass with a natural MORB composition collected from the Mid-Atlantic Ridge (runs #71 and #75). The same starting material was used in our previous experiments (Hirose et al., 1999; Hirose & Fei, 2002; Hirose et al., 2005). Subducted MORB material may not be identical to the original one due to dehydration on subduction. However, since the major element chemistry is not strongly affected by this process (Schneider & Eggler, 1986), our natural MORB glass should be well representative of subducted oceanic crust composition. In addition, we prepared another glass with a composition of the MORB + 15 wt% $CaSiO_3$ doped with Nd and Sm to investigate Ca-pv/melt element partitioning in runs CP01 to CP07. The starting mixture was prepared from analytical grade oxides and carbonates. The dried and decarbonated reagents were ground together under acetone in a mortar. The mixture was loaded into a graphite capsule, and fused at 1600 K and 1.5 GPa for 1 hr in a piston-cylinder apparatus. The concentrations of Nd and Sm were found to be ~3,700 μg/g in this starting material from the subsequent LA-ICP-MS analysis.

High-pressure melting experiments were conducted using laser-heated DAC techniques. The glass starting material was powdered and pressed into a disk with a typical thickness of 15 to 25 μm and placed into a sample chamber without thermal insulation layers. No additional metal laser absorber was used. The sample was compressed with beveled 150 μm or flat 300 μm culet diamond anvils, depending on a target pressure. Heating was performed from both sides of the sample by employing two 100 W single-mode Yb fiber lasers (*SPI* or *IPG photonics*) with beam shaping optics (*New focus*) that converts a beam with a Gaussian intensity distribution to the one with a flat-top distribution. The laser spot size was 20 to 40 μm on a sample. Heated duration ranged from 3 to 10 s except time series experiments. Since sample temperature was not obtained in runs #71 and #75, it was estimated from melt fraction and the solidus and liquidus temperature of MORB material (Andrault, Pesce, et al., 2014) with the uncertainty of ±10% (Tateno et al., 2014), assuming that the degree of partial melting increases linearly with increasing temperature between the solidus and the liquidus (Takahashi et al., 1993; Table 1). For the runs CP01 to CP07, temperatures were measured using a spectroradiometric method, and one-dimensional radial temperature profile across a laser-heated spot was obtained. The measured temperatures at the interfaces between solid and liquid were averaged to obtain the experimental temperature and its uncertainty, combined with the texture of a sample cross section (e.g., Tateno et al., 2018). For the run CP05, we assume the same experimental temperature as that in the run CP06 where the same laser power was used, because the temperature measurements were failed.

Phase identification was made by synchrotron XRD measurements at BL10XU, SPring-8 in runs #71 and #75 (Ohishi et al., 2008). The XRD patterns were collected on an imaging plate with exposure time of 5 min. A monochromatic incident X-ray beam was focused by stacked compound refractive lenses and collimated to approximately 6-μm area (full-width of half maximum) on a sample. The wavelengths used were 0.4136(1) and 0.4143(1) Å (~30 keV) in runs #71 and #75, respectively. Visible fluorescence light from diamond excited by X-rays was used to precisely align a laser-heated spot with the X-ray beam. Two-dimensional XRD images were integrated as a function of two-theta angle in order to produce conventional one-dimensional diffraction patterns using the IP Analyzer program (Seto et al., 2010). Sample pressures after laser heating were determined from the unit-cell volume of silica phases and their equations of state (runs #71 and #75)

Table 1
Experimental Conditions and Results

Run	Starting material	*P* (GPa)	*T* (K)[a]	*t* (s)	Phase assemblage in crystallization sequence[b]
#75	MORB	72	3700*	3	Melt (59) → Ca-pv (19) → $CaCl_2$-type SiO_2(8) → MgPv (14)
#71		135	4300*	3	Melt (51) → Ca-pv (20) → PPv (24) → Seifertite(5)
CP01	MORB +15% $CaSiO_3$ + Nd, Sm	32	2570 (100)	10	Melt → Ca-pv → SiO_2 → CAS → MgPv
CP02		52	2940 (140)	10	Melt → Ca-pv → SiO_2
CP03		69	3280 (130)	10	Melt → Ca-pv → SiO_2
CP05		31	2510*	2	Melt → Ca-pv → SiO_2
CP06		35	2510 (100)	5	Melt → Ca-pv → SiO_2
CP07		33	2420 (170)	1	Melt → Ca-pv → SiO_2

[a]Asterisks denote estimated temperature due to failure of temperature measurement (see the text for details). Numbers in parentheses indicate errors in the last digits. [b]Ca-pv, $CaSiO_3$-perovskite; MgPv, $MgSiO_3$-rich perovskite; PPv, postperovskite; CAS, calcium aluminosilicate. Number in parentheses are phase proportions (wt%) calculated by mass balance.

(Andrault, Trønnes, et al., 2014) or Raman peak shift of a diamond anvil (runs CP01 to CP07; Akahama & Kawamura 2004). A thermal pressure contribution was added by +2.5 GPa/1000 K (Andrault et al., 2011).

2.2. Analytical Techniques

2.2.1. Electron Microprobe Analysis

Textural and chemical characterizations were made on quenched samples. After complete pressure release, the sample was recovered from a DAC and glued on a silicon wafer using polymeric resin. Subsequently, it was polished by an Ar ion beam in an Ion Slicer (JEOL EM-09100 IS) to minimize damage on sample surface (Tateno, Sinmyo, et al., 2009), allowing us to observe microtextures of an extremely tiny sample. The section was carefully thinned to 10 μm thickness such that the center of a heating spot was exposed from both sides parallel to the compression and laser-heating axis. Such polished sample sections were examined with an FE-EPMA (JEOL JXA-8530F) with acceleration voltage of 10 kV and beam current of 12 nA. We collected X-ray maps for Si, Ti, Al, Fe, Mn, Mg, Ca, Na, K, and Cr for each sample. The chemical composition of quenched liquid pool was obtained with defocused electron beams of 5-μm size to avoid potential local heterogeneity, and that of neighboring Ca-pv was analyzed by focused beam with a spatial resolution of <2 μm. Counting time was 20 s on a peak and 10 s on background except 10 and 5 s for Na and K.

2.2.2. TEM Analysis

After the bulk sample analysis with FE-EPMA, we milled the samples from runs #71 and #75 thin enough for electron beam transparency. The site-specific milling on a heated portion was provided by a focused Ga ion beam (FIB; FEI Versa™ 3D DualBeam™) operating at 30 kV and 5 nA (1.5 pA for final surfacing). Chemical analyses were made with energy-dispersive X-ray spectrometry (EDS) using a field-emission type scanning TEM (JEOL JEM-2800) operated at 200 kV. The chemical compositions of individual phases of Mg-pv, postperovskite, Ca-pv, and SiO_2 phase in these thin film samples were determined based on a *k*-factor method (Cliff & Lorimer, 1975); $C_i/C_{Si} = k_i\,(I_i/I_{si})$, where *C* and *I* are concentrations and X-ray counts, respectively, for element i and Si. The *k*-factor for each element i (k_i) was determined by using a natural alkaline basaltic glass as a standard (SiO_2 = 51.34%, TiO_2 = 1.70%, Al_2O_3 = 15.87%, FeO = 7.91%, MnO = 0.16%, MgO = 7.06%, CaO = 10.45%, Na_2O = 3.55%, K_2O = 0.28%, and P_2O_5 = 0.22% in weight).

In order to evaluate the thickness dependence of a *k*-factor, we prepared three wedge-shaped thin films with different thickness by the Ion Slicer and subsequent FIB millings as described above. Figure 1 shows the variation in calculated *k*-factors as a function of total X-ray intensity that reflected the film thickness. For elements exhibiting no clear dependence on the film thickness, we obtained the *k*-factor by averaging the values obtained. For Fe, Al, and Mg, on the other hand, we assumed liner relations between their *k*-factors and the film thickness to correct the effect of thickness (Fujino et al., 1998). The data were scattered for Mn, Na, and K likely because of their low concentrations. In order to validate these, the thin films of natural alkali feldspar (Na_2O = 7.07% and K_2O = 5.62% in weight) and synthetic $MnSiO_3$ were also prepared in a similar manner. The *k*-factors obtained from these samples were in very good agreement with those from the alkaline basalt.

Ga implantation into a thin film by FIB milling could lead to possible overestimation of the Na content in a phase because the Ga *L*α line is very close in energy to the Na *K*α line. However, we did not detect any

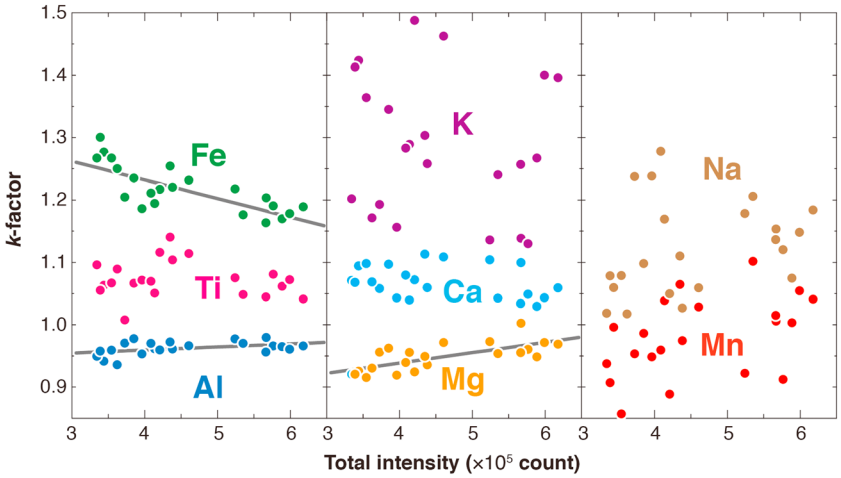

Figure 1. The variation of *k*-factor for each element as a function of total X-ray intensity corresponding to thickness of a thin foil. The chemical compositions of individual phase were determined based on the k-factor method (Cliff & Lorimer, 1975). Thickness correction was made assuming simple linear relation for Al, Fe, and Mg (Fujino et al., 1998).

EDS signals at the corresponding energies for the $CaCl_2$-type SiO_2 in the run #75, while the neighboring Mg-pv exhibits high Na_2O content of 2.72 wt% (Table 2). It suggests that serious Ga contamination is not likely to occur by our procedure for the thin film preparation.

2.2.3. LA-ICP-MS Analysis

The Nd and Sm abundances in recovered CP01 to CP03 samples were determined by an LA-ICP-MS at the Kyoto University. The analyses were performed using 193 nm ArF excimer lasers (New Wave) coupled with a quadrupole-based ICP-MS (Thermo Scientific iCAP Q; e.g., Iizuka & Hirata, 2004; Orihashi & Hirata, 2003). The ablation cell was flushed with helium, leading to enhanced sensitivity (Eggins et al., 1998; Guillong & Günther, 2002). Laser ablation was employed with energy of 2.6–4.0 J/cm^2 and repetition rate of 5 Hz. Laser beam spots were 2 and 10 μm in diameter for analyzing Ca-pv and quenched partial melts, respectively. The analysis was performed for isotopes of ^{44}Ca, ^{146}Nd, and ^{147}Sm. The Ca concentration determined by electron microprobe was used as an internal standard for processing Nd and Sm data. The reference NIST 610 glass was used as a calibration standard (Pearce et al., 1997). Time-resolved spectra were obtained to monitor signal intensity for all masses simultaneously. Background gas blank was measured for ~60 s before every shot on a sample for ~25 s.

3. Results

3.1. Phase Relations in MORB

Melting experiments on MORB were conducted at 72 GPa and 3700 K (run #75) and 135 GPa and 4300 K (run #71; Table 1). The crystallization sequence below the liquidus was determined from the position of the nearly monomineralic zones of Ca-pv, silica, and Mg-pv relative to the central melt pool. The chemical compositions of partial melt and solids are given in Table 2, together with phase proportions based on mass balance calculations.

3.1.1. 72 GPa (Run #75)

After quenching temperature from 72 GPa, microscope observation through a diamond anvil showed a concentric texture at 62 GPa and 300 K; a transparent area surrounded an opaque portion located at the center (Figure 2).

Such texture reflected a temperature distribution (hottest at the center) during laser heating and is similar to those observed in our previous melting experiments on $(Mg_{0.9}Fe_{0.1})_2SiO_4$ and a pyrolitic material in a DAC (Nomura et al., 2011; Tateno et al., 2014). Figure 3a demonstrates an XRD pattern collected mainly from the transparent area, indicating a mineral assemblage of Ca-pv + Mg-pv + $CaCl_2$-type silica phase. We then examined the cross section of this sample parallel to the compression/laser-heating axis with an FE-EPMA. Figure 4 represents a back-scattered electron image and X-ray maps. A round central pocket of quenched

Journal of Geophysical Research: Solid Earth

10.1029/2018JB015790

Table 2
Chemical Compositions of Starting Material and Coexisting Phases for MORB Experiment[a]

Sample		72 GPa, 3700 K (run#75)								135 GPa, 4300 K (run#71)								
Phase[b]	SM	Melt		Ca-pv		$CaCl_2$-type SiO_2		MgPv		Melt		Ca-pv		PPv		Seifertite		Restite[f]
Analysis		EPMA		EPMA		TEM-EDS		TEM-EDS		EPMA		TEM-EDS		TEM-EDS		TEM-EDS		
n[c]		16		10		6		6		10		6		3		3		
wt%																		
SiO_2	49.64	44.26	(0.83)	50.95	(0.40)	91.31	(0.39)	43.34	(1.98)	42.60	(1.14)	51.86	(0.27)	50.51	(0.49)	92.02	(1.14)	55.3
TiO_2	1.64	2.14	(0.16)	0.70	(0.07)	0.11	(0.13)	1.89	(0.33)	2.45	(0.21)	0.66	(0.12)	0.79	(0.11)	0.07	(0.08)	0.7
Al_2O_3	14.88	18.29	(0.55)	2.65	(0.27)	6.79	(0.78)	18.47	(0.95)	17.95	(0.51)	1.73	(0.27)	18.15	(0.80)	6.30	(0.31)	10.2
FeO[d]	11.43	14.58	(1.35)	2.42	(0.36)	0.59	(0.25)	12.20	(0.93)	16.70	(1.47)	2.58	(0.03)	6.92	(0.31)	0.43	(0.12)	4.5
MnO	0.18	0.21	(0.07)	0.09	(0.07)	0.08	(0.09)	0.94	(0.33)	0.24	(0.07)	0.05	(0.01)	0.12	(0.06)	0.03	(0.03)	0.1
MgO	8.51	9.03	(0.27)	3.26	(0.31)	0.74	(0.57)	16.31	(1.26)	7.05	(0.12)	2.90	(0.25)	17.34	(0.58)	0.82	(0.47)	9.8
CaO	10.55	4.53	(0.26)	35.63	(0.73)	0.34	(0.36)	4.02	(0.72)	3.84	(0.25)	38.27	(0.27)	1.69	(0.23)	0.20	(0.16)	16.5
Na_2O	2.90	2.35	(0.18)	1.22	(0.12)	-		2.72	(0.26)	1.43	(0.42)	1.37	(0.14)	4.44	(0.09)	0.13	(0.12)	2.7
K_2O	0.12	0.16	(0.04)	0.22	(0.04)	0.05	(0.09)	0.12	(0.10)	0.10	(0.04)	0.59	(0.09)	0.04	(0.04)	-		0.3
Cr_2O_3		0.12	(0.06)	0.02	(0.03)	-		-		0.15	(0.01)	-		-		-		
Total	99.85	95.67	(1.30)	97.17	(0.79)	100		100		92.49	(0.76)	100		100		100		100
Proportion[e]		59		19		8		14		51		20		24		5		
O = 24																		
Si		6.75		7.93		11.13		6.32		6.77		7.93		7.04		11.20		7.87
Ti		0.25		0.08		0.01		0.21		0.29		0.08		0.08		0.01		0.07
Al		3.29		0.49		0.97		3.18		3.36		0.31		2.98		0.90		1.72
Fe		1.86		0.31		0.06		1.49		2.22		0.33		0.81		0.04		0.53
Mn		0.03		0.01		0.01		0.12		0.03		0.01		0.01		0.00		2.07
Mg		2.05		0.76		0.13		3.55		1.67		0.66		3.60		0.15		2.51
Ca		0.74		5.95		0.04		0.63		0.65		6.27		0.25		0.03		0.76
Na		0.69		0.37		-		0.77		0.44		0.41		1.20		0.03		0.05
K		0.03		0.04		0.01		0.02		0.02		0.12		0.01		-		0.01
Cr		0.01		0.00		-		-		0.02		-		-		-		-
Sum		15.71		15.95		12.37		16.28		15.48		16.10		15.99		12.36		15.60

[a]Numbers in parenthesis are one standard deviation in the last digits. [b]SM, starting material; Ca-pv, $CaSiO_3$-perovskite; MgPv, $MgSiO_3$-rich perovskite; PPv, postperovskite. [c]Number of analyses. [d]All Fe was assumed to be ferrous. [e]Phase proportions (wt%) were calculated by mass balance. [f]Calculated by the mixture of Ca-pv (41 wt%), PPv (49 wt%), and seifertite (10 wt%).

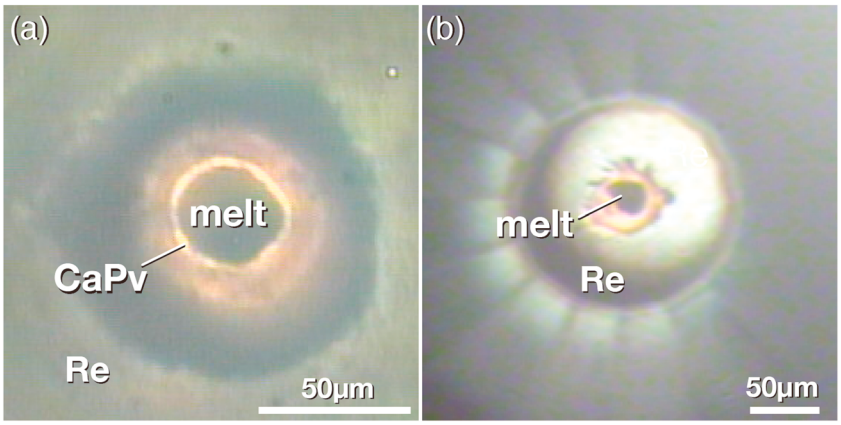

Figure 2. Microscope images after melting obtained at (a) 62 GPa (run#75) and (b) 125 GPa at 300 K (run#71). Opaque melt pools were formed after melting at the center of the hot spot surrounded by transparent Ca-perovskite (Ca-pv) zone.

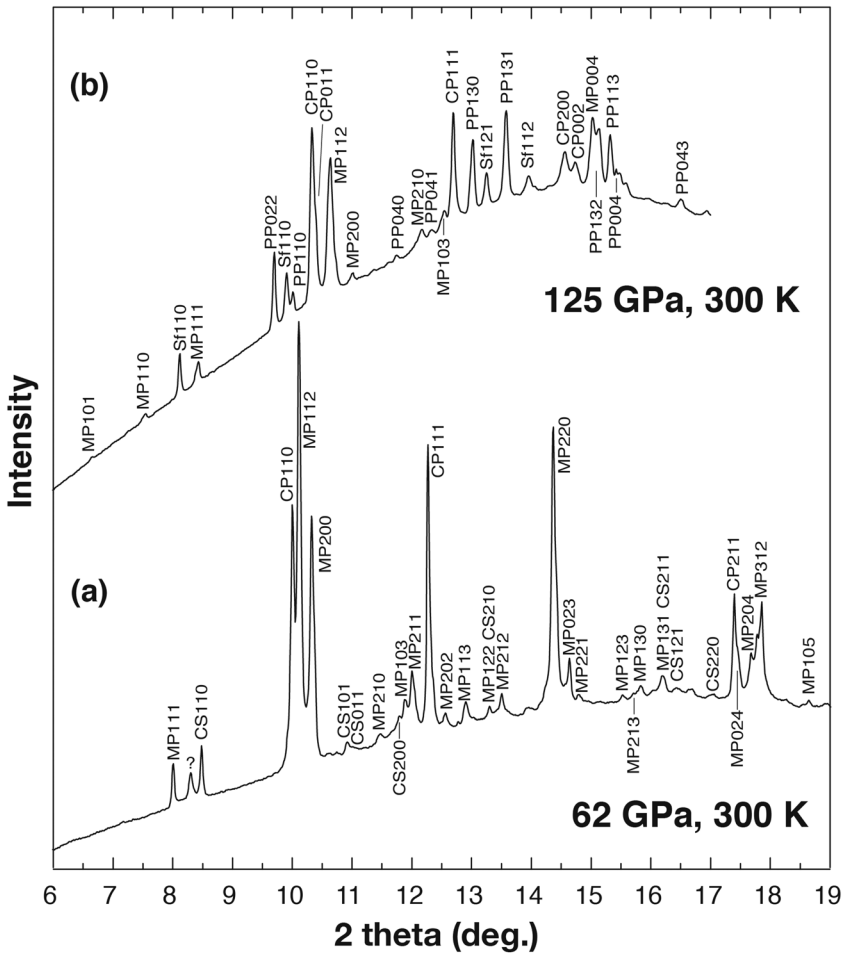

Figure 3. X-ray diffraction patterns of a MORB composition collected after melting at (a) 62 GPa (run#75, λ = 0.4143(1) Å) and (b) ~~125 GPa~~ (run#71, λ = 0.4136(1) Å). CP, $CaSiO_3$-perovskite; MP, $MgSiO_3$-rich perovskite; PP, postperovskite; CS, $CaCl_2$-type SiO_2 phase; Sf, seifertite (αPbO_2-type SiO_2).

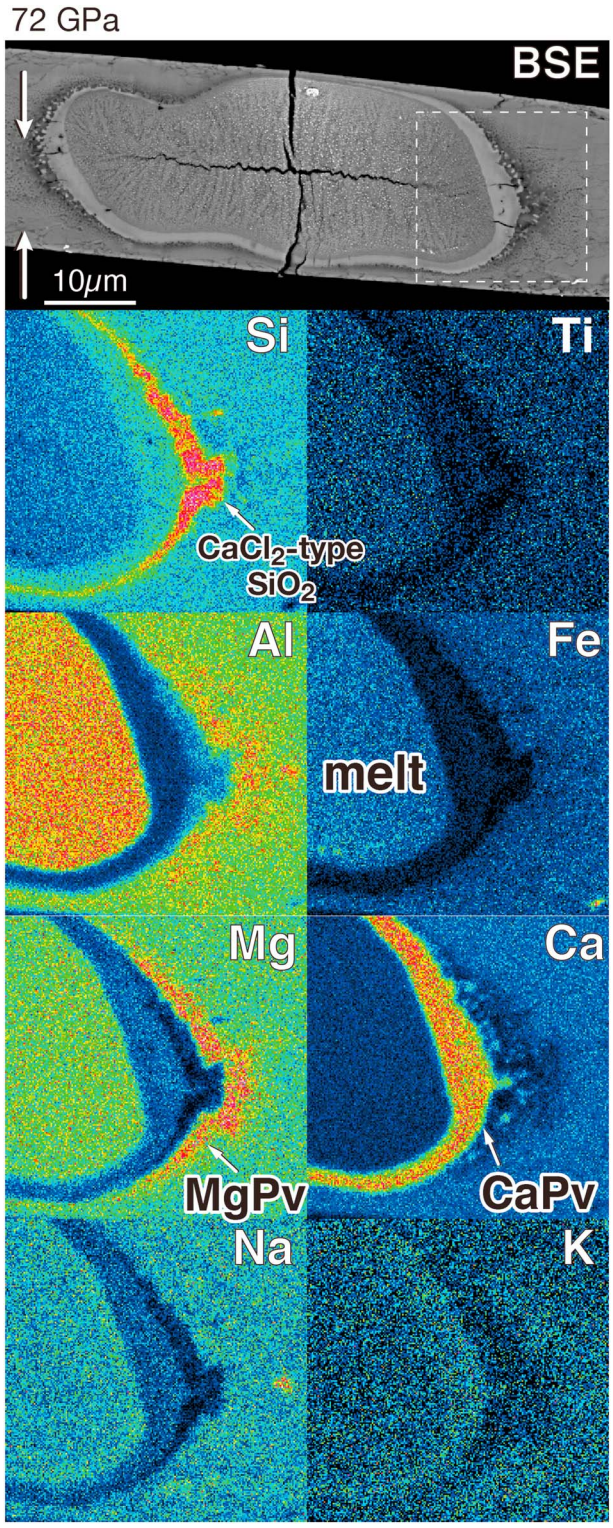

Figure 4. Backscattered electron (BSE) image and magnified X-ray elemental maps of a boxed area for the sample recovered from 72 GPa (run #75). Quenched partial melt is found at the center of the sample, where temperature was the highest. Melt pocket is enclosed by a zone of single-phase $CaSiO_3$-perovskite (Ca-pv), the liquidus phase, followed by $CaCl_2$-type SiO_2, and $MgSiO_3$-perovskite (MgPv). The arrows show the directions of laser beams for heating from both sides of the sample.

melt with nonstoichiometric composition and strong iron enrichment is surrounded by a Ca-rich zone, identified as Ca-pv by quantitative analysis. An intermediate zone with a Si-dominated phase and an outer Mg-rich phase are present outside the Ca-pv zone.

In order to obtain the textures, spatial relationships, and chemical compositions of the solid phases, we also prepared a thin foil for TEM analysis with an FIB technique. The obtained TEM images (Figure 5a) confirmed the zonation of the phases. Si-rich and Mg-rich phases observed by FE-EPMA were identified to be SiO_2 and Mg-pv with EDS/TEM. Both of them were converted to amorphous as well as unquenchable Ca-pv, which likely occurred during ion millings. The X-ray maps indicated that the zones outside the Ca-pv are not monomineralic but include mixed phases. The silica-rich phase starts to appear associated with Ca-pv, and then Mg-pv joins the assemblage further down the temperature gradient (Figure 5b). Such zoning (phase segregation) has been commonly observed in previous multianvil and DAC experiments and interpreted to represent a crystallization sequence with decreasing temperature; see Trønnes and Frost (2002), Hirose and Fei (2002), Ito et al. (2004), and Liebske et al. (2005) for multianvil studies and Nomura et al. (2011), Tateno et al. (2014), and Pradhan et al. (2015) for DAC experiments. In this manner, the melting texture of the present DAC experiment at 72 GPa (Figures 4 and 5) demonstrates that Ca-pv is the liquidus phase and is followed by $CaCl_2$-type SiO_2 and then by Mg-pv, with decreasing temperature.

The X-ray elemental maps obtained outside the Mg-rich zone shows a subsolidus phase assemblage (Figure 5c). This low-temperature part of the sample includes an Al-rich phase, probably of the calcium ferrite (CF) type structure and stoichiometry, in addition to Mg-pv, Ca-pv, and $CaCl_2$-type silica. The grain sizes in the subsolidus part of the sample, however, are too small to determine the chemical composition of each phase. Such a subsolidus phase assemblage is consistent with that observed in previous experiments on MORB materials (Hirose et al., 2005; Ricolleau et al., 2010).

3.1.2. 135 GPa (Run #71)

The optical microscope image of the 135 GPa experimental product also shows an opaque portion at the center of the laser-heated spot (Figure 2b). The XRD pattern obtained from the zone between opaque and surrounding transparent areas contains reflections from postperovskite, Mg-pv, seifertite (α-PbO_2-type SiO_2), and tetragonal Ca-pv (Figure 3b). Microprobe analysis demonstrates that the chemical composition of the opaque melt pocket is nonstoichiometric with enrichment in both Fe and Al. X-ray maps obtained with FE-EPMA show that the quenched partial melt is surrounded by Ca-rich phase, followed by Mg-rich and then Si-rich phases (Figure 6). The individual phases are more clearly resolved in the X-ray maps collected by EDS/TEM (Figure 7), confirming that Ca- and Si-rich phases are Ca-pv and seifertite, respectively. Only seifertite was preserved as a crystalline phase, and the others were amorphous when observed under the TEM. The Mg-rich phase contained substantial amount of Na_2O (4.44 ± 0.09 wt%), similar to postperovskite with 5.0 wt% Na_2O in MORB (Hirose et al., 2005). This suggests that the Mg-rich phase is postperovskite rather than Mg-pv, which is also supported by the fact that the experiment was performed at 135 GPa and >4000 K, within the

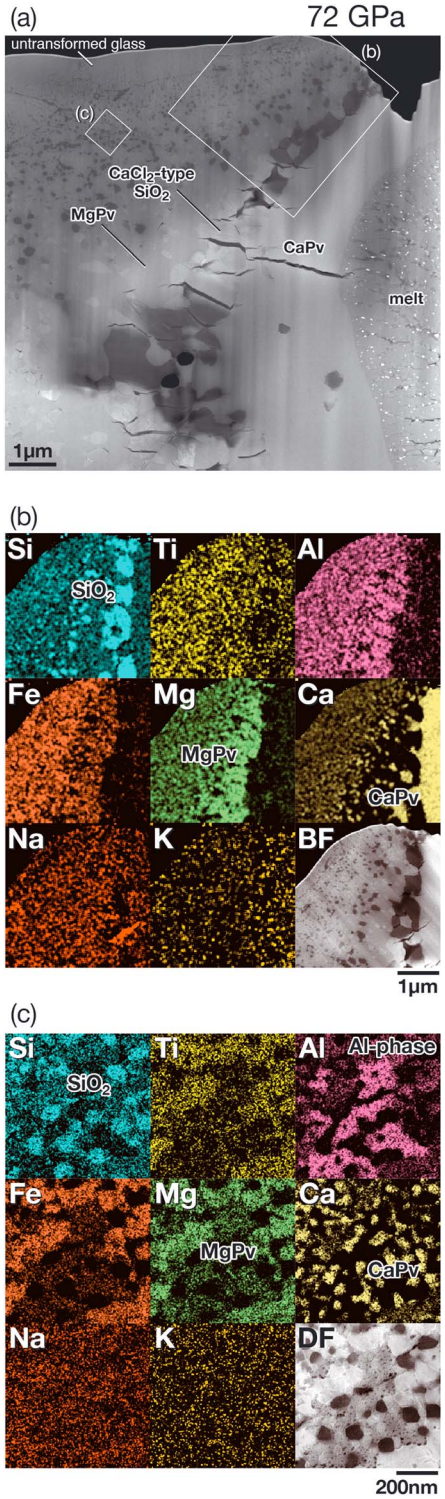

Figure 5. (a) TEM darkfield image of the boxed area for the sample run#75 obtained at 72 GPa after FE-EPMA analysis shown in Figure 4. The darkfield image gives the atomic number contrast (*Z*); the bright areas correspond to high *Z* values. (b) X-ray maps corresponding to the boxed area in (a). Crystallization sequence is found to be $CaSiO_3$-perovskite (Ca-pv), $CaCl_2$-type SiO_2, and $MgSiO_3$-perovskite (MgPv) along temperature gradient. (c) Aggregate of MgPv, Ca-pv, aluminous phase (Al-phase), and SiO_2 observed at lower temperature region likely under subsolidus condition.

stability field of postperovskite in MORB (Andrault, Pesce, et al., 2014; Grocholski et al., 2012; Hirose et al., 2005; Ohta et al., 2008). Mg-pv found in the XRD pattern is likely attributed to quench crystals formed in the melt pool. We did not observe other phases than Ca-pv, seifertite, and postperovskite outside the melt pool.

In contrast, previous subsolidus experiments on MORB showed the presence of CF-type phase that is enriched in both Na and Al (Grocholski et al., 2012; Hirose et al., 2005; Ohta et al., 2008). The difference may be due to the high temperature in this study compared to 2000 to 2800 K in the previous experiments. Hirose et al. (2005) measured high concentrations of Al_2O_3 in postperovskite, Ca-pv, and seifertite (12.1, 4.2, and 12.6 wt%, respectively) from a 113 GPa experiment.

A small Fe metal pool was found in the silicate melt portion (Figure 6). It included SiO_2 blobs, similar to those observed in recent liquid-metal/liquid-silicate partitioning experiments in a DAC (e.g., Fischer et al., 2015; Siebert et al., 2012). It suggests that liquid metal pool was present during heating.

3.2. Partitioning Between Ca-pv and Melt

This study confirms that Ca-pv is the liquidus phase in MORB to the lowermost mantle (Hirose & Fei, 2002; Pradhan et al., 2015). We examined element partitioning between Ca-pv and melt from 31 to 69 GPa in runs CP01 to CP07 (Tables 1 and 3), using a synthetic MORB glass doped with $CaSiO_3$, Sm, and Nd as starting material. Recovered samples were first characterized by FE-EPMA. We obtained Ca-pv/melt partition coefficient *D* for Ti, Fe, Mg, Na, and K from weight concentrations in coexisting Ca-pv and melt. Time series experiments were carried out at 31–35 GPa and 2420–2510 K by changing heating duration from 1 to 10 s (Table 3). Figure 8 shows the variations in obtained partition coefficients as a function of heating duration. No remarkable variations were observed after 1–2 s, suggesting that the length scales is very short in a DAC sample, and hence, the selected heating duration of 10 s was sufficient for equilibrium. Ca-pv dissolves at the hottest central part and precipitates at the liquidus temperature along thermal gradient due to saturation gradient chemical diffusion, which results in the complete separation of liquid from crystals (Lesher & Walker, 1988). In this process, precipitating Ca-pv is in chemical equilibrium with neighboring liquid.

Subsequently, we determined D_{Nd} and D_{Sm} on the basis of the LA-ICP-MS analyses (Figure 9). The addition of $CaSiO_3$ component to the starting material resulted in the crystallization of a larger amount of Ca-pv. The Ca-pv zone was thus wide enough for laser ablation with a spot size of 2 μm. A 10 μm beam size was used to analyze quenched melt pools. A laser beam always penetrated through the sample with ~10 μm thickness. We always checked whether the laser sampled only Ca-pv or partial melt by examining the backside of the sample. Data were discarded when the laser hits neighboring other phases. The variations in Nd and Sm concentrations in quenched partial melts were typically less than ±10%, indicating their homogeneous distributions (Table 3). On the other hand, relatively large variations were obtained for Ca-pv.

Partition coefficients for alkali elements (sodium and potassium) obtained in the experiments on both natural and doped MORB

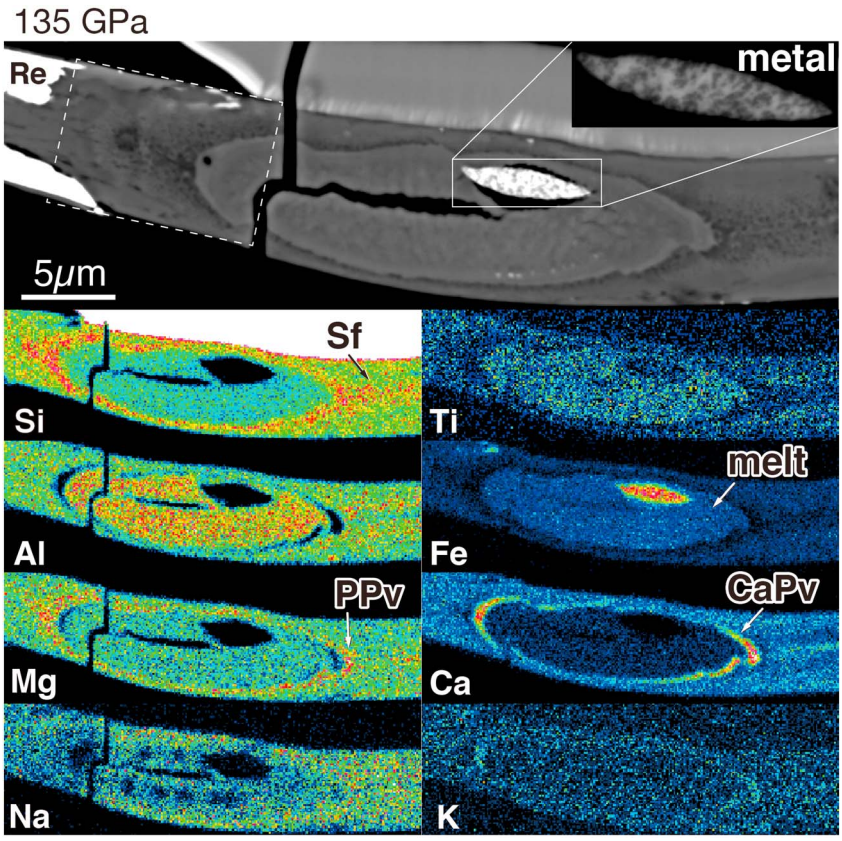

Figure 6. Backscattered electron images and X-ray maps for the sample at 135 GPa (run #71), in which $CaSiO_3$-perovskite (Ca-pv) is as a liquidus phase, followed by postperovskite (PPv), and seifertite (Sf). Liquid iron metal was found in silicate melt (boxed area with a different brightness and contrast). Re, rhenium gasket.

materials show a substantial pressure effect (Figure 10a). The D_{Na} and D_K values monotonically increase with increasing pressure, reaching unity at 135 and 70 GPa for Na and K, respectively. The pressure effect is more significant for potassium, which changes by more than an order of magnitude from D_K = 0.3 at 30 GPa to D_K = 6 at 135 GPa. Potassium is incompatible in Ca-pv at the uppermost lower mantle, while highly compatible in the CMB region. On the contrary, D_{Nd} and D_{Sm} exhibit moderately negative pressure dependence (Figure 10b). It is noted that the D_{Sm}/D_{Nd} becomes smaller at higher pressure, eventually less than unity, although error bars are relatively large. Nd could be more compatible than Sm at the CMB, while it is opposite up to the uppermost lower mantle pressures (e.g., Corgne et al., 2005; Hirose et al., 2004; Figure 10b).

4. Discussion

4.1. Crystallization Sequence in MORB

The subsolidus and melting phase relations of MORB through the lower mantle pressure range are summarized in Figure 11. Earlier melting experiments demonstrated that the liquidus phase changes from majorite garnet to Ca-pv above 23 GPa (Hirose & Fei, 2002; Yasuda et al., 1994). At the highest pressure of 27.5 GPa ever studied for melting of MORB in a multianvil press, melt crystallizes Ca-pv, stishovite, calcium alminosilicate (CAS) phase, Mg-pv, and CF-type Al-rich phase with decreasing temperature above solidus (Hirose & Fei, 2002). The CAS phase is not included in the subsolidus phase assemblage and forms as a consequence of incongruent melting (Hirose et al., 1999).

A more recent study based on a combination of DAC experiment and TEM analysis demonstrated the crystallization sequence to be Ca-pv → stishovite → Mg-pv at 58 and 101 GPa (Pradhan et al., 2015). We observed the similar sequence of Ca-pv → $CaCl_2$-type SiO_2 → Mg-pv at 72 GPa in this study. The CAS phase was absent

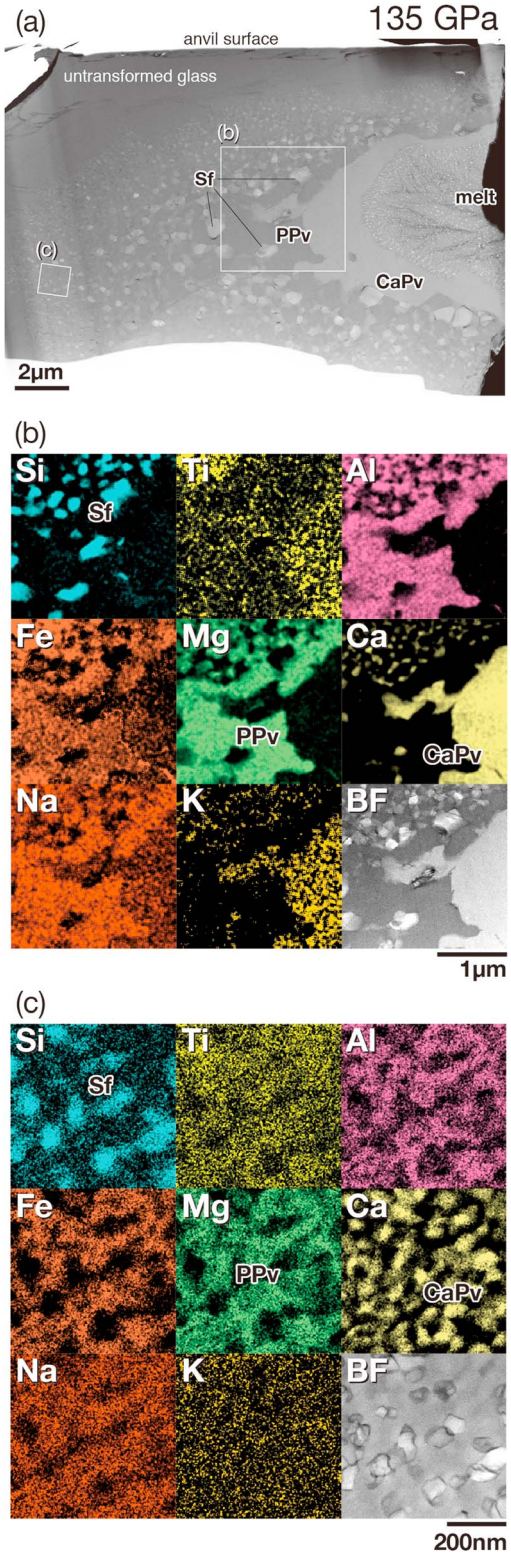

Figure 7. (a) TEM darkfield image of the boxed areas for the sample run#71 obtained at 135 GPa followed by FE-EPMA analysis in Figure 6. (b) X-ray maps for the boxed area in (a). $CaSiO_3$-perovskite (Ca-pv) found in a direct contact with the liquid, and sequential zones of seifertite (Sf) and postperovskite (PPv) toward the anvil surface. (c) Three phase aggregate of Ca-pv, PPv, and Sf at lower temperature region.

because it is not stable above 35 GPa (Ishibashi et al., 2008). The CF-type Al-phase should appear when temperature decreases to right above the solidus temperature. The phase transformation from Mg-pv to postperovskite has been shown to occur between 112 and 118 GPa at 2500 K by Ohta et al. (2008) or between 109 and 123 GPa by Grocholski et al. (2012).

At 135 GPa in the stability field of postperovskite in MORB, the present experiment demonstrate that Ca-pv remains to be the liquidus phase, followed by postperovskite and SiO_2 seifertite. Postperovskite appears at higher temperature than that for the silica phase, while Mg-pv starts to crystallize at lower temperature than that for SiO_2 at 70 GPa in this study and below 101 GPa in Pradhan et al. (2015) (Figure 11). It is consistent with the previous XRD measurements by Andrault, Pesce, et al. (2014), who reported that the silica phase melted in advance of Mg-pv with increasing temperature at 120 GPa.

4.2. Partial Melts of MORB

Melts obtained at 70 and 135 GPa in this study were formed by 59 and 51 wt% partial melting of MORB (Table 2). They contain 43–46 wt% SiO_2, 15–17 wt% FeO, and ~4 wt% CaO, close to the melts formed by similar degrees of partial melting (56–66 wt%) at 27–27.5 GPa in earlier multianvil experiment (Hirose & Fei, 2002). The MgO content decreases remarkably from 12.4 wt% at the upper-most lower mantle pressure to 7.1 wt% at the CMB condition, which is expected from the stabilization of Mg-pv (and postperovskite as well) relative to the SiO_2 phases within the melting range with increasing pressure (Figure 11).

Based on in situ XRD measurements and scanning electron microscope analyses of recovered samples, however, Andrault, Pesce, et al. (2014) found more SiO_2 and less FeO in the central hot spot with increasing pressure. They argued that a partial melt formed in the deep lower mantle is more SiO_2-rich than those found at lower pressures. Partial melts make a pool at the hottest part of a laser-heated sample. Although this is in broad agreement with the silica-Mg-pv eutectic relations in the system MgO-SiO_2 (de Koker et al., 2013), it is possible that enrichment in SiO_2 in partial melt located in the hot area is a consequence of the Soret effect, causing migration of Si and Fe toward the high- and low-temperature parts, respectively. It is also noted that the geometry where Andrault and others employed the chemical analyses is strikingly different from that presented in Pradhan et al. (2015) and this study; while we made cross-sectional observation parallel to the heating and compression axis, they examined the surface of recovered sample disks after removal of KCl pressure medium.

Iron enrichment in partial melts is a key factor that controls the buoyancy of partial melts in the deep lower mantle (Stixrude et al., 2009; Sun et al., 2011; Thomas et al., 2012). The present experiment indicate that the partial melt of MORB is remarkably enriched in FeO (Table 2; Pradhan et al., 2015), suggesting that it is likely to be denser than the surrounding mantle at the CMB. Indeed, based on Funamori and Sato (2010), who demonstrated a sink/float relationship between Mg-pv and melt as a function of Fe/(Mg + Fe) ratio and SiO_2 content in melt, our partial MORB melt obtained at 135 GPa should be denser than the surrounding solid mantle.

Table 3
Chemical Compositions of Starting Material and Coexisting Phases for CP Series[a]

Run				CP01				CP02				CP03			
P (GPa)				32				52				69			
T (K)				2570 (100)				2940 (140)				3280 (130)			
Phase[b]		SM		Melt		Ca-pv		Melt		Ca-pv		Melt		Ca-pv	
FE-EPMA															
	n[c]	8		15		2		8		4		3		7	
wt%	SiO_2	50.62	(0.17)	45.16	(1.13)	45.26	(0.53)	44.84	(1.12)	48.77	(0.32)	46.78	(1.21)	49.49	(0.58)
	TiO_2	1.23	(0.09)	1.92	(0.21)	0.77	(0.06)	1.78	(0.12)	0.84	(0.18)	1.68	(0.22)	0.65	(0.19)
	Al_2O_3	12.14	(0.18)	15.12	(1.54)	4.22	(0.09)	20.48	(1.45)	2.11	(0.17)	21.98	(2.18)	1.70	(0.39)
	FeO*	8.26	(0.41)	15.09	(2.62)	1.71	(0.01)	13.79	(2.79)	1.95	(0.31)	13.69	(2.39)	1.94	(0.20)
	MgO	6.80	(0.11)	10.55	(0.41)	2.34	(0.12)	9.20	(0.55)	2.52	(0.52)	8.12	(0.23)	2.30	(0.29)
	CaO	16.27	(0.29)	6.03	(0.44)	38.08	(0.21)	5.53	(1.86)	35.96	(0.97)	5.22	(1.39)	36.06	(0.59)
	Na_2O	2.11	(0.09)	3.17	(0.21)	0.41	(0.02)	2.79	(0.17)	0.46	(0.12)	2.49	(0.08)	0.47	(0.08)
	K_2O	1.00	(0.06)	1.18	(0.10)	0.28	(0.01)	1.18	(0.05)	0.68	(0.19)	1.06	(0.11)	0.86	(0.09)
	Total	98.43	(0.72)	98.21	(1.25)	93.05	(0.69)	99.60	(2.23)	93.30	(0.95)	101.03	(2.92)	93.47	(0.73)
O = 24	Si	7.51		6.89		7.47		6.60		7.94		6.72		8.04	
	Ti	0.14		0.21		0.10		0.20		0.10		0.18		0.08	
	Al	2.12		2.57		0.82		3.55		0.40		3.72		0.32	
	Fe	1.03		1.81		0.24		1.69		0.27		1.64		0.26	
	Mg	1.50		2.27		0.57		2.02		0.61		1.74		0.56	
	Ca	2.59		1.31		6.73		0.88		6.28		0.81		6.28	
	Na	0.61		0.88		0.13		0.79		0.15		0.69		0.15	
	K	0.19		0.22		0.06		0.22		0.14		0.19		0.18	
	Sum	15.69		16.16		16.12		15.94		15.89		15.69		15.88	
LA-ICP-MS															
	n[c]	4		4		3		3		1		3		3	
μg/g	Nd	3686	(42)	675	(58)	10933	(744)	901	(68)	11971	-	930	(21)	8871	(665)
	Sm	3703	(75)	585	(59)	10318	(728)	763	(89)	10873	-	883	(31)	7890	(529)

[a]Numbers in parenthesis are one standard deviation in the last digits. [b]SM, starting material; Ca-pv, $CaSiO_3$-perovskite. [c]Number of analyses.

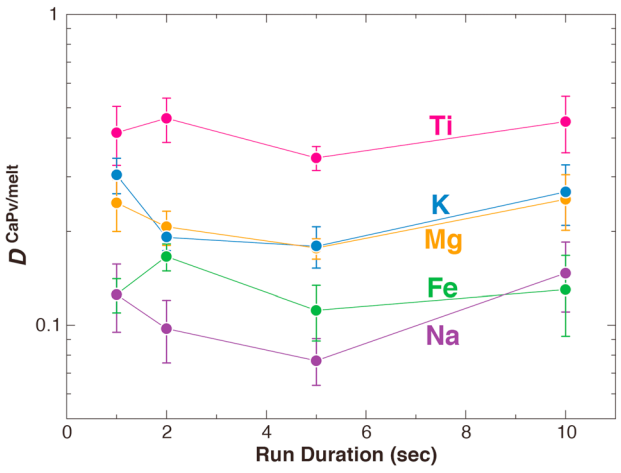

Figure 8. The result for a time series experiment (CP01, CP05–07) of partition coefficients between Ca-perovskite and melt carried out at 32–35 GPa and 2420–2570 K. No remarkable variations were observed up to 10 s.

4.3. Ca-pv/Melt Partitioning in the Lower Mantle

We investigated the Ca-pv/melt partition coefficients (log *D*) for Na, K to 135 GPa and for Nd, and Sm to 69 GPa (Figure 10). A large positive pressure effect on the D_{Na} and D_K makes these elements compatible in Ca-pv ($D > 1$) at the lowermost mantle conditions. Partial melts of MORB would therefore be depleted in these alkali elements when residual solids are predominantly Ca-pv at sufficiently high degrees of partial melting. The D_K value, in particular, increases by a factor of 20 with increasing pressure from 30 to 140 GPa (Figure 10a). An increase in partition coefficients for monovalent cations with increasing pressure was reported for olivine/melt, clonopyroxine/melt, and majorite garnet/melt (Imai et al., 2012; Suzuki et al., 2012; Taura et al., 1998; Wang & Takahashi, 1999). Moreover, Tateno et al. (2014) on the basis of melting experiments on a pyrolitic mantle material found that D_{Na} for Mg-pv/melt also monotonically increases from 0.07 at 34 GPa to 0.21 at 88 GPa. Such pressure effect is reasonably explained by the high compressibility of large monovalent cations, which are more compressible than cations with higher valences (Hazen and Finger, 1979; Blundy & Wood, 1994). Reduced ionic radius for such cations, which are

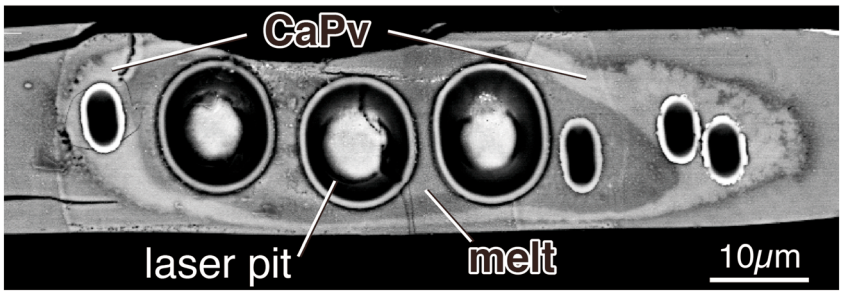

Figure 9. Backscattered electron image obtained after LA-ICP-MS analysis on the sample recovered from 69 GPa and 3280 K. Laser-spot sizes of 2 and 10-μm are used for $CaSiO_3$-perovskite (Ca-pv) and melt, respectively.

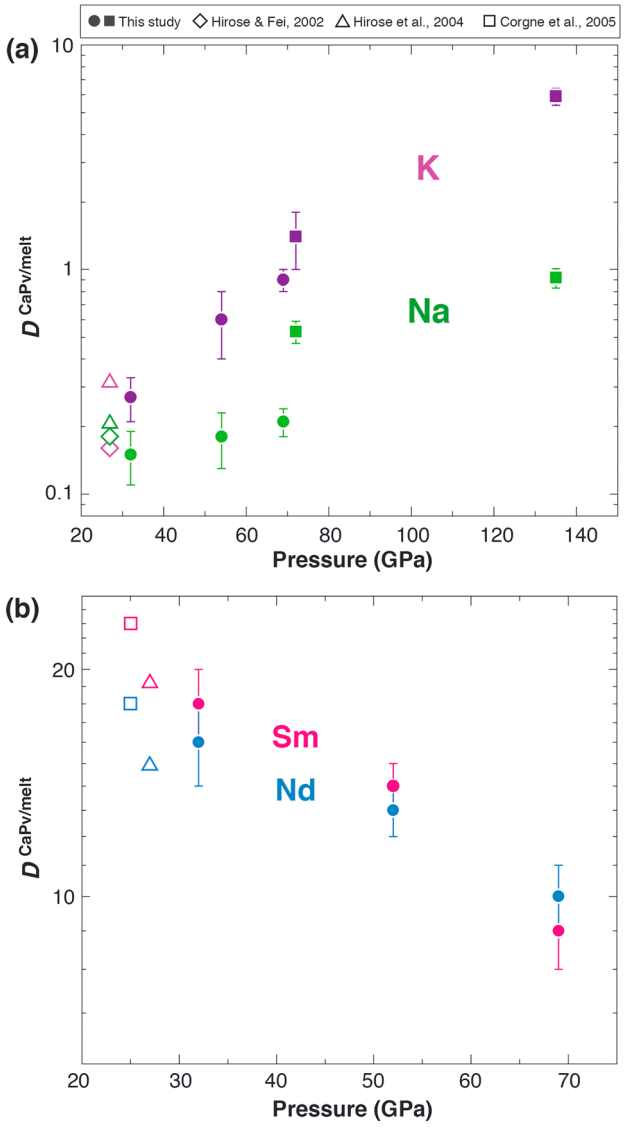

Figure 10. Pressure effect on partition coefficients between $CaSiO_3$-perovskite and melt for (a) Na and K and (b) Nd and Sm together with earlier studies by multianvil experiments (open symbol; Corgne et al., 2005; Hirose et al., 2004; Hirose & Fei, 2002). The filled circle and square denote the data obtained at runs CP01–03 and #71 and #75, respectively.

generally incompatible at low to moderate pressures, may make them more compatible in the crystal sites at high pressure. On the other hand, the partition coefficients of Nd and Sm decreased with increasing pressure, since they are relatively incompressive trivalent cations. Pressure effect on the crystal/melt partition coefficient is a consequence from different compressibility between crystal lattice site and ionic radius (Suzuki et al., 2012). Also, it is likely controlled also by a change in the structure of melt upon compression. More systematic study is necessary to clarify this issue.

Superchondritic $^{142}Nd/^{144}Nd$ (high Sm/Nd) ratios observed in terrestrial rocks may require a complementary reservoir with low Sm/Nd ratios (e.g., Caro, 2011). This study shows that Ca-pv/melt partition coefficients are higher than ~10 for both Nd and Sm in the uppermost 880 km of the lower mantle (Figure 10). Both are partitioned preferentially into Ca-pv rather than the other major lower mantle phases of Mg-pv and ferropericlase (Corgne et al., 2005; Hirose et al., 2004), and Ca-pv plays a key role in the differentiation of large ion lithophile elements including Nd and Sm when melting occurs in the lower mantle (Caro et al., 2005). We found in this study (Figure 10b) that D_{Sm}/D_{Nd} becomes smaller with pressure and finally less than unity in the deep lower mantle pressure. It suggests that melting of materials rich in Ca-pv does not help formation of the low Sm/Nd complementary reservoir.

4.4. Fate of Solid Residue After MORB Melting

It has been argued that the source mantle for oceanic island basalts shows trace element signatures that were inherited from Ca-pv- and Mg-pv-bearing precursors (Collerson et al., 2010; Hanyu et al., 2011; Hirose et al., 2004). Such precursors may be solid residues from partial melting of subducted MORB materials in the D" layer. Ca-pv, constituting 25 mol% of a subsolidus MORB assemblage but only 5–8% of a pyrolite assemblage (e.g., Murakami et al., 2005; Hirose et al., 2005; Irifune et al., 2010; Stixrude & Lithgow-Bertelloni, 2012), is the liquidus phase in MORB, which has a lower solidus temperature than pyrolitic mantle (Hirose et al., 1999; Andrault, Pesce, et al., 2014).

We calculated a density profile of a residual solid (restite) formed by 51% partial melting of MORB (Figure 12). A mass balance calculation yields the proportion of each phase in the residue, whose chemical composition was obtained by TEM-EDS analysis: 41 wt% Ca-pv, 49 wt% postperovskite, and 10 wt% seifertite (Table 2). Subsequently,

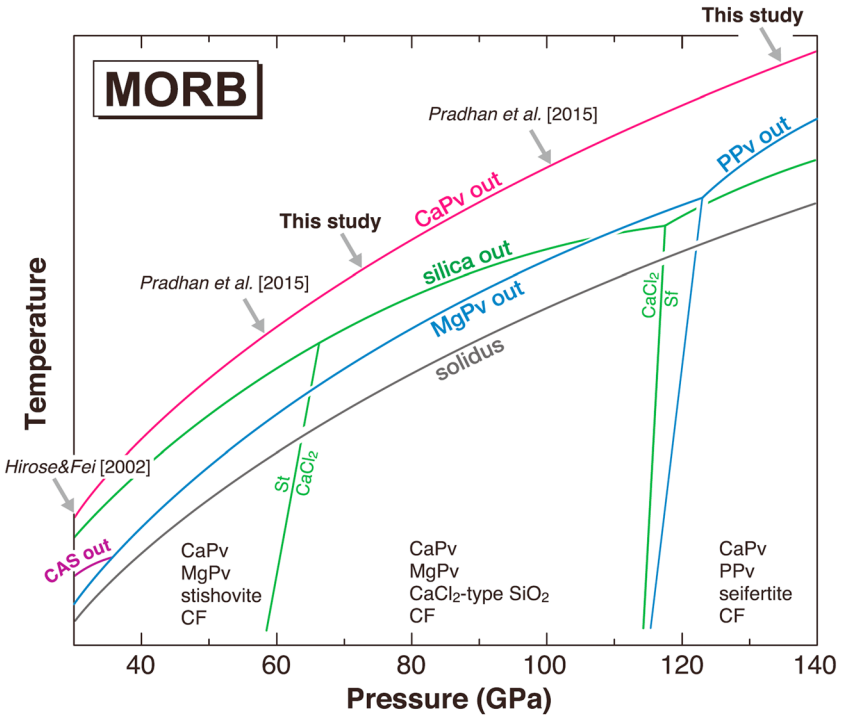

Figure 11. Summary of subsolidus and melting phase relations of MORB composition. $CaSiO_3$-perovskite (Ca-pv) is a first liquidus phase throughout the lower mantle. The melting relations are constrained based on this study and previous studies (Hirose & Fei, 2002; Pradhan et al., 2015). The Al-phase is absent above 35 GPa due to a breakdown of calcium alminosilicate (CAS) phase (Ishibashi et al., 2008). The melting sequence changes at ~100 GPa where the second liquidus phase changes from silica to $MgSiO_3$-perovskite (MgPv)/postperovskite (PPv). The subsolidus phase boundaries are from the literatures (Andrault, Trønnes, et al., 2014; Grocholski et al., 2013; Hirose et al., 2005; Nomura et al., 2010).

we calculated the density of each phase using its unit-cell volume from XRD data collected from the resite part of the sample (transparent portion surrounding the dark iron-rich quenched melt portion; Figure 2b) and the measured chemical compositions. The restite densities were obtained along hot geotherm, by employing elastic and thermal parameters from known equations of state for the constituent minerals, Mg-pv and Ca-pv (Ricolleau et al., 2010), postperovskite (Sakai et al., 2016), and the silica phases (Wang et al., 2012; Andrault, Trønnes, et al., 2014). Here we considered phase transformations during decompression from postperovskite to Mg-pv and from seifertite to $CaCl_2$-type SiO_2 and further to stishovite. The hot geotherm was simply assumed to be 200 K higher than the normal geotherm (Omori & Komabayashi, 2007), anchored by postspinel and postperovskite phase transitions (Ito & Katsura, 1989; Tateno, Hirose, et al., 2009). The temperature profile inside the bottom thermal boundary layer was also from Tateno, Hirose, et al. (2009). The density of unmelted MORB rock, which comprises Mg-pv/postperovskite, Ca-pv, silica phases, and CF phase, is calculated in a similar manner, using available equation of state data (Ricolleau et al., 2010; Sakai et al., 2016; Wang et al., 2012) and the mineral proportions and chemical compositions at the lowermost mantle condition, reported in Hirose et al. (2005).

The calculated density of the restite formed by 51 wt% partial melting of MORB is higher than the PREM value (Dziewonski & Anderson, 1981) at the bottom thermal boundary layer largely due to dense postperovskite (Figure 12a). Throughout the stability range of Mg-pv, the restite density is nearly identical to that of PREM (Figure 12b). At low degrees of partial melting, the restite density is close to that of MORB, which is ~5% denser than the surrounding mantle. When the degree of partial melting is high, the restite should be strongly enriched in Ca-pv, which has slightly higher denser than PREM (Hirose et al., 2005; Ricolleau et al., 2010; Figure 12b). Although MORB restites generally have high density in the lower mantle, the restites from partial melting of about 50% have densities within 1.5% of the surrounding mantle. Such restites with geochemical signatures characteristic of Ca-pv may easily become entrained in a convecting mantle (Collerson et al., 2010; Hanyu et al., 2011; Hirose et al., 2004).

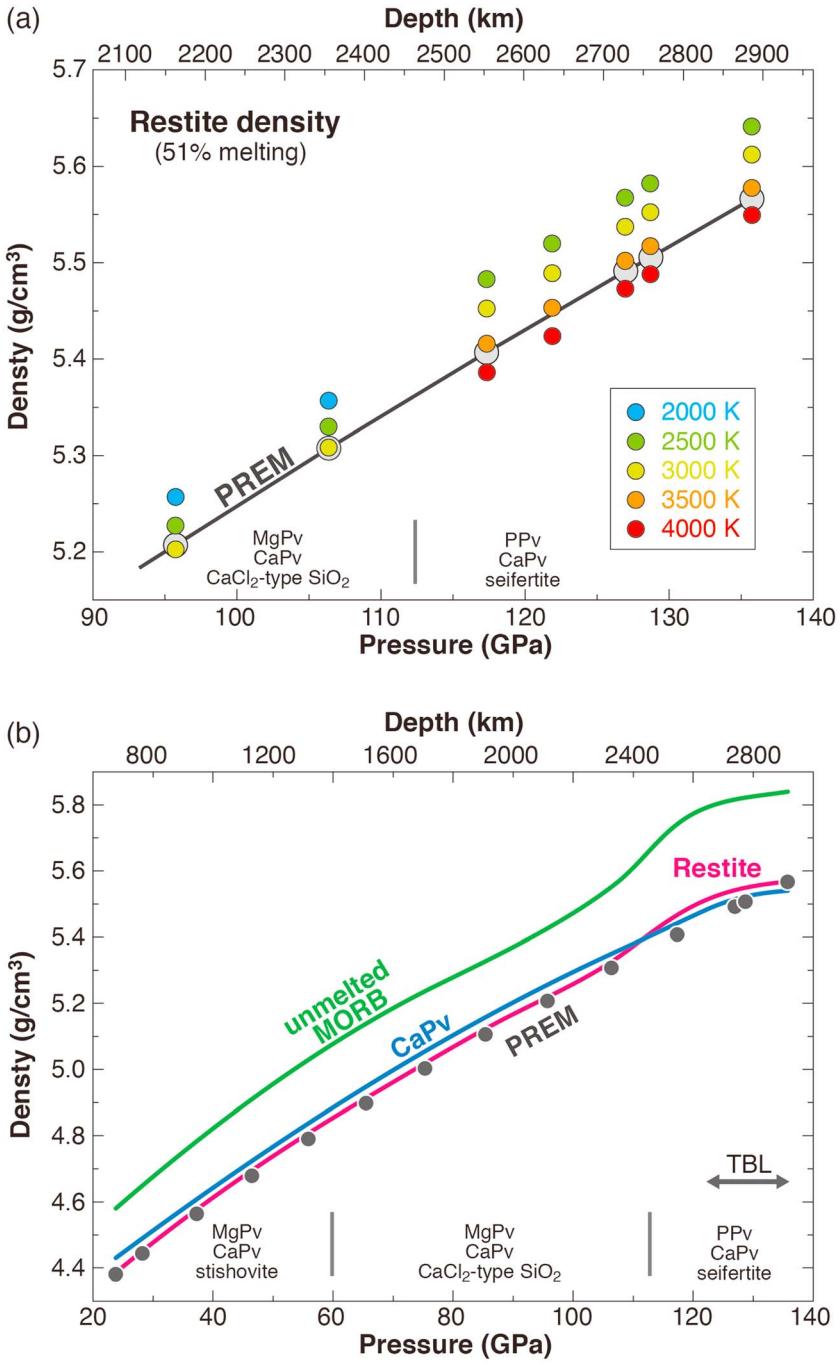

Figure 12. Calculated densities of bulk restite from 51% melting of MORB. The restite is composed of Ca-pv (41%), MgPv/PPv (49%), and silica (10%). (a) Densities calculated by using corresponding equations of state at different temperature are plotted together with PREM density (see the detail in the text). (b) Density profiles of bulk restite along a hot geotherm. The temperatures inside the bottom thermal boundary layer (TBL) are also considered. Unmelted MORB and Ca-pv are shown as references for no melting and for melting degrees exceeding 51%, respectively. The restite density is greater than PREM through the entire lower mantle pressure range, except in the D″ zone (the TBL).

5. Summary and Conclusion

Melting phase relations of a MORB material and the element partitioning between Ca-pv and melts were examined up to 135 GPa, corresponding to the conditions at base of the mantle. We found the following:

1. Ca-pv is the liquidus phase and therefore also the last phase to melt throughout the lower mantle pressure range.
2. Whereas the silica phase, stishovite, and modified stishovite ($CaCl_2$-structure type) crystallize as the second liquidus phase below the liquidus phase up to more than 100 GPa (Pradhan et al., 2015), postperovskite appears to crystallize slightly before seifertite in our 135 GPa experiment.
3. The partial melts of MORB are strongly enriched in FeO and depleted in SiO_2.
4. The pressure effect on element partitioning is large.

Since Ca-pv/melt partition coefficients for K, and possibly also for Na, become larger than unity at CMB, they are no longer incompatible elements during partial melting of MORB. The D_{Nd} and D_{Sm} for Ca-pv/melt equilibria decrease substantially with increasing pressure. Since they become similar to each other and the D_{Sm}/D_{Nd} approaches unity (possibly decrease below unity) in the deep lower mantle, it is not likely that the low Sm/Nd reservoir complementary to superchondritic $^{142}Nd/^{144}Nd$ (high Sm/Nd) mantle is formed by deep mantle melting of materials rich in Ca-pv. Protracted crystal fractionation of Mg-pv from a basal magma ocean, however, might produce residual enriched melts with low Sm/Nd ratios (e.g., Walter et al., 2004; Liebske et al., 2005; Corgne et al., 2005). Melt formed by ~50% partial melting of MORB shows marked iron-enrichment and is thus denser than surrounding mantle above the CMB. On the other hand, the density of residual solid is calculated to be very close to the PREM density, suggesting that the MORB restite can be easily entrained in a convective flow and recycled to the surface. The observed pressure effect on Ca-pv/melt partitioning implies that solid residues enriched in Ca-pv, formed by partial melting of MORB in the deep lower mantle, might have low Sm/Nd ratios.

Acknowledgments
Reidar G. Trønnes and an anonymous reviewer are acknowledged for their constructive comments, which greatly improved manuscript. Synchrotron XRD measurements were conducted at BL10XU, SPring-8 (proposal no. 2010A0087). We are grateful to Toshihiro Suzuki and Tetsuya Komabayashi for fruitful discussions about element partitioning and phase relation. We also thank Eiichi Takahashi for the use of a piston-cylinder apparatus in his laboratory. This work was supported in part by JSPS KAKENHI grant 21224013 to T. H. The data that support the conclusions presented in this manuscript are either provided in the data tables and figures or is properly cited and referred to in the reference list.

References

Akahama, Y., & Kawamura, H. (2004). High pressure Raman spectroscopy of diamond anvils to 250 GPa: Method for pressure determination in the multimegabar pressure range. *Journal of Applied Physics*, *96*(7), 3748–3751. https://doi.org/10.1063/1.1778482

Andrault, D., Bolfan-Casanova, S., Lo Nigro, N. G., Bouhifd, M. A., Garbarino, G., & Mezouar, M. (2011). Solidus and liquidus profiles of chondritic mantle: Implication for melting of the Earth across its history. *Earth and Planetary Science Letters*, *304*(1-2), 251–259. https://doi.org/10.1016/j.epsl.2011.02.006

Andrault, D., Pesce, G., Bouhifd, M. A., Bolfan-Casanova, N., Hénot, J.-M., & Mezouar, M. (2014). Melting of subducted basalt at the core–mantle boundary. *Science*, *344*, 892–895. https://doi.org/10.1126/science.1250466

Andrault, D., Trønnes, R. G., Konôpková, Z., Morgenroth, W., Liermann, H. P., Morard, G., & Mezouar, M. (2014). Phase diagram and *P-V-T* equation of state of Al-bearing seifertite at lowermost mantle conditions. *American Mineralogist*, *99*(10), 2035–2042, https://doi.org/10.2138/am-2014-4697

Blundy, J. D., & Wood, B. J. (1994). Prediction of crystal-melt partition coefficients from elastic moduli. *Nature*, *372*(6505), 452–454. https://doi.org/10.1038/372452a0

Caro, G. (2011). Early silicate Earth differentiation. *Annual Review of Earth and Planetary Sciences*, *39*(1), 31–58. https://doi.org/10.1146/annurev-earth-040610-133400

Caro, G., Bourdon, B., Wood, B. J., & Corgne, A. (2005). Trace element fractionation generated by melt segregation from a magma ocean. *Nature*, *436*(7048), 246–249. https://doi.org/10.1038/nature03827

Cliff, G., & Lorimer, G. W. (1975). The quantitative analysis of thin specimens. *Journal of Microscopy*, *103*(2), 203–207. https://doi.org/10.1111/j.1365-2818.1975.tb03895.x

Collerson, K. D., Williams, Q., Ewart, A. E., & Murphy, D. T. (2010). Origin of HIMU and EM-1 domains sampled by ocean island basalts, kimberlites and carbonatites: The role of CO_2-fluxed lower mantle melting in thermochemical upwellings. *Physics of the Earth and Planetary Interiors*, *181*, 112–131. https://doi.org/10.1016/j.pepi.2010.05.008

Corgne, A., Liebske, C., Wood, B. J., Rubie, D. C., & Frost, D. J. (2005). Silicate perovskite-melt partitioning of trace elements and geochemical signature of a deep perovskitic reservoir. *Geochimica et Cosmochimica Acta*, *69*(2), 485–496. https://doi.org/10.1016/j.gca.2004.06.041

de Koker, N., Karki, B. B., & Stixrude, L. N. (2013). Thermodynamics of the MgO–SiO_2 liquid system in Earth's lowermost mantle from first principles. *Earth and Planetary Science Letters*, *361*, 58–63. https://doi.org/10.1061/j.epsl.2012.11.026

Dziewonski, A. M., & Anderson, D. L. (1981). Preliminary reference Earth model. *Physics of the Earth and Planetary Interiors*, *25*, 297–356. https://doi.org/10.1016/0031-9201(81)90046-7

Eggins, S., Kinsley, L., & Shelley, J. (1998). Deposition and element fractionation processes during atmospheric pressure laser sampling for analysis by ICP-MS. *Applied Surface Science*, *127–129*, 278–286. https://doi.org/10.1016/S0169-4332(97)00643-0

Fischer, R. A., Nakajima, Y., Campbell, A. J., Frost, D. J., Harries, D., Langenhorst, F., et al. (2015). High pressure metal–silicate partitioning of Ni, Co, V, Cr, Si, and O. *Geochimica et Cosmochimica Acta*, *167*, 177–194. https://doi.org/10.1016/j.gca.2015.06.026

Fujino, K., Miyajima, N., Yagi, T., Kondo, T., & Funamori, N. (1998). Analytical electron microscopy of the garnet-perovskite transformation in a laser-heated diamond anvil cell. In M. H. Manghnani, & T. Yagi (Eds.), *Properties of Earth and Planetary Materials at High Pressure and Temperature*, *Geophys. Monogr. Ser.*, (Vol. 101, pp. 409–417). Washington, D. C: American Geophysical Union. https://doi.org/10.1029/GM101p0409

Funamori, N., & Sato, T. (2010). Density contrast between silicate melts and crystals in the deep mantle: An integrated view based on static-compression data. *Earth and Planetary Science Letters*, *295*(3-4), 435–440. https://doi.org/10.1016/j.epsl.2010.04.021

Garnero, E. J., & Helmberger, D. V. (1995). A very slow basal layer underlying large-scale low-velocity anomalies in the lower mantle beneath the Pacific: Evidence from core phases. *Physics of the Earth and Planetary Interiors*, *91*(1-3), 161–176. https://doi.org/10.1016/0031-9201(95)03039-Y

Grocholski, B., Catalli, K., Shim, S.-H., & Prakapenka, V. (2012). Mineralogical effects on the detectability of the postperovskite boundary. *Proceedings of the National Academy of Sciences*, *109*(7), 2275–2279. https://doi.org/10.1073/pnas.1109204109

Grocholski, B., Shim, S.-H., & Prakapenka, V. B. (2013). Stability, metastability, and elastic properties of a dense silica polymorph, seifertite. *Journal of Geophysical Research: Solid Earth*, *118*, 4745–4757. https://doi.org/10.1002/jgrb.50360

Guillong, M., & Günther, D. (2002). Effect of particle size on ICP-induced elemental fractionation on laser ablation-inductively coupled plasma-mass spectrometry. *Journal of Analytical Atomic Spectrometry*, *17*(8), 831–837. https://doi.org/10.1039/B202988J

Hanyu, T., Tatsumi, Y., Senda, R., Miyazaki, T., Chang, Q., Hirahara, Y., et al. (2011). Geochemical characteristics and origin of the HIMU reservoir: A possible mantle plume source in the lower mantle. *Geochemistry, Geophysics, Geosystems*, *12*, Q0AC09. https://doi.org/10.1029/2010GC003252

Hazen, R. M., & Finger, L. W. (1979). Bulk modulus-volume relationship for cation-anion polyhedra. *Journal of Geophysical Research*, *84*, 6723–6728. https://doi.org/10.1029/JB084iB12p06723

Hirose, K., & Fei, Y. (2002). Subsolidus and melting phase relations of basaltic composition in the uppermostlower mantle. *Geochimica et Cosmochimica Acta*, *66*(12), 2099–2108. https://doi.org/10.1061/S0016-7037(02)00847-5

Hirose, K., Fei, Y., Ma, Y., & Mao, H. -K. (1999). The fate of subducted basaltic crust in the Earth's lower mantle. *Nature*, *397*, 53–56. https://doi.org/10.1038/16225

Hirose, K., Shimizu, N., van Westrenen, W., & Fei, Y. (2004). Trace element partitioning in Earth's lower mantle and implications for geochemical consequences of partial melting at the core–mantle boundary. *Physics of the Earth and Planetary Interiors*, *146*(1-2), 249–260. https://doi.org/10.1061/j.pepi.2002.11.001

Hirose, K., Takafuji, N., Sata, N., & Ohishi, Y. (2005). Phase transition and density of subducted MORB crut in the lower mantle. *Earth and Planetary Science Letters*, *237*(1–2), 239–251. https://doi.org/10.1016/j.epsl.2005.06.035

Iizuka, T., & Hirata, T. (2004). Simultaneous determinations of U-Pb age and REE abundances of zircon crystals using ArF Eximer laser ablation-inductively coupled plasma-mass spectrometry equipped with a Chicane ion lens system. *Geochemical Journal*, *38*(3), 229–241. https://doi.org/10.2343/geochemj.38.229

Ishibashi, K., Hirose, K., Sata, N., & Ohishi, Y. (2008). Dissociation of the CAS phase in the uppermost lower mantle. *Physics and Chemistry of Minerals*, *35*, 197–200. https://doi.org/10.1007/s00269-007-0212-4

Imai, T. E., Takahashi, T., Suzuki, T., & Hirata, T. (2012). Element partitioning between olivine and melt up to 10 GPa: Implications for the effect of pressure. *Physics of the Earth and Planetary Interiors*, *212–213*, 64–75. https://doi.org/10.1061/j.pepi.2002.11.001

Irifune, T., & Ringwood, A. E. (1993). Phase transformations in subducted oceanic crust and buoyancy relationships at depths of 600–800 km in the mantle. *Earth and Planetary Science Letters*, *117*(1-2), 101–110. https://doi.org/10.1016/0012-821X(93)90120-X

Irifune, T., Shinmei, T., McCammon, C. A., Miyajima, N., Rubie, D. C., & Frost, D. J. (2010). Iron partitioning and density changes of pyrolite in Earth's lower mantle. *Science*, *327*(5962), 193–195. https://doi.org/10.1126/science.1181443

Ito, E., & Katsura, T. (1989). A temperature profile of the mantle transition zone. *Geophysical Research Letters*, *16*(5), 425–428. https://doi.org/10.1029/GL016i005p00425

Ito, E., Kubo, A., Katsura, T., & Walter, M. J. (2004). Melting experiments of mantle materials under lower mantle conditions with implications for magma ocean differentiation. *Physics of the Earth and Planetary Interiors*, *143–144*, 397–406. https://doi.org/10.1016/j.pepi.2003.09.016

Komiya, T. (2004). Material circulation model including chemical differentiation within the mantle and secular variation of temperature and composition of the mantle. *Physics of the Earth and Planetary Interiors*, *146*(1-2), 333–367. https://doi.org/10.1016/j.pepi.2003.03.001

Lay, T., Garnero, E. J., & Williams, Q. (2004). Partial melting in a thermo-chemical boundary layer at the base of the mantle. *Physics of the Earth and Planetary Interiors*, *146*(3-4), 441–467. https://doi.org/10.1016/j.pepi.2004.04.004

Lesher, C. E., & Walker, D. (1988). Cumulate maturation and melt migration in a temperature gradient. *Journal of Geophysical Research*, *93*, 10295. https://doi.org/10.1029/JB093iB09p10295

Liebske, C., Corgne, A., Frost, D. J., Rubie, D. C., & Wood, B. J. (2005). Compositional effects on element partitioning between Mg-silicate perovskite and silicate melts. *Contributions to Mineralogy and Petrology*, *149*(1), 113–128. https://doi.org/10.1007/s00410-004-0641-8

Murakami, M., Hirose, K., Sata, N., & Ohishi, Y. (2005). Post-perovskite phase transition and mineral chemistry in the pyrolitic lowermost mantle. *Geophysical Research Letters*, *32*, L03304. https://doi.org/10.1029/2004GL021956

Nomura, R., Hirose, K., Nagayoshi, S., & Ohishi, Y. (2010). Precise determination of post-stishovite phase transition boundary and implications for seismic heterogeneities in the mid-lower mantle. *Physics of the Earth and Planetary Interiors*, *183*, 104–109. https://doi.org/10.1016/j.pepi.2010.08.004

Nomura, R., Ozawa, H., Tateno, S., Hirose, K., Hernlund, J., Muto, S., et al. (2011). Spin crossover and iron-rich silicate melt in the Earth's deep mantle. *Nature*, *473*(7346), 199–202. https://doi.org/10.1038/nature09940

Ohishi, Y., Hirao, N., Sata, N., Hirose, K., & Takata, M. (2008). Highly intense monochromatic X-ray diffraction facility for high-pressure research at SPring-8. *High Pressure Research*, *28*(3), 163–173. https://doi.org/10.1080/08957950802208910

Ohta, K., Hirose, K., Lay, T., Sata, N., & Ohishi, Y. (2008). Phase transitions in pyrolite and MORB at lowermost mantle conditions: Implications for a MORB-rich pile above the core–mantle boundary. *Earth and Planetary Science Letters*, *267*(1-2), 107–117. https://doi.org/10.1016/j.epsl.2007.11.037

Omori, S., & Komabayashi, T. (2007). Subduction zone: The water channel to the mantle. In D. Yuen, S. Maruyama, S. Karato, & B. Windley (Eds.), *Superplumes: Beyond Plate Tectonics*, (pp. 113–138). Netherlands: Springer. https://doi.org/10.1007/978-1-4020-5750-2_5

Ono, S., Ito, E., & Katsura, T. (2001). Mineralogy of subducted basaltic crust (MORB) from 25 to 37 GPa, and chemical heterogeneity of the lower mantle. *Earth and Planetary Science Letters*, *190*(1-2), 57–63. https://doi.org/10.1016/S0012-821X(01)00375-2

Orihashi, Y., & Hirata, T. (2003). Rapid quantitative analysis of Y and REE abundances in XRF glass bead for selected GSJ reference rock standards using Nd-YAG 266 nm UV laser ablation ICP-MS. *Geochemical Journal*, *37*(3), 401–412. https://doi.org/10.2343/geochemj.37.401

Pearce, N., Perkins, W., Westgate, J., Gorton, M., Jackson, S., Neal, C., & Chenery, S. (1997). A complication of new and published major and trace element data for NIST SRM 610 and NIST SRM 612 glass reference materials. *Geostandards Newsletter*, *21*(1), 115–144. https://doi.org/10.1111/j.1751-908X.1997.tb00538.x

Pradhan, G. K., Fiquet, G., Siebert, J., Auzende, A. -L., Morard, G., Antonangeli, D., & Garbarino, G. (2015). Melting of MORB at core–mantle boundary. *Earth and Planetary Science Letters*, *431*, 247–255. https://doi.org/10.1016/j.epsl.2015.09.034

Ricolleau, A., Perrillat, J. -P., Fiquet, G., Daniel, I., Matas, J., Addad, A., et al. (2010). Phase relations and equation of state of a natural MORB: Implications for the density profile of subducted oceanic crust in the Earth's lower mantle. *Journal of Geophysical Research*, *115*, B08202. https://doi.org/10.1029/2009JB006709

Sakai, T., Dekura, H., & Hirao, N. (2016). Experimental and theoretical thermal equations of state of $MgSiO_3$ post-perovskite at multi-megabar pressures. *Scientific Reports*, *6*(1), 22652. https://doi.org/10.1038/srep22652

Schneider, M. E., & Eggler, D. H. (1986). Fluids in equilibrium with peridotite minerals: Implications for mantle metasomatism. *Geochimica et Cosmochimica Acta*, *50*(5), 711–724. https://doi.org/10.1016/0016-7037(86)90347-9

Seto, Y., Nishio-Hamane, D., Nagai, T., & Sata, N. (2010). Development of a software suite on X-ray diffraction experiments. *Review of High Pressure Science and Technology*, *20*(3), 269–276. https://doi.org/10.4131/jshpreview.20.269

Siebert, J., Badro, J., Antonangeli, D., & Ryerson, F. J. (2012). Metal–silicate partitioning of Ni and co in a deep magma ocean. *Earth and Planetary Science Letters*, *321–322*, 189–197. https://doi.org/10.1016/j.epsl.2012.01.013

Stixrude, L., de Koker, N., Sun, N., Mookherjee, M., & Karki, B. B. (2009). Thermodynamics of silicate liquids in the deep Earth. *Earth and Planetary Science Letters*, *278*(3-4), 226–232. https://doi.org/10.1061/j.epsl.2008.12.006

Stixrude, L., & Lithgow-Bertelloni, C. (2012). Geophysics of chemical heterogeneity in the mantle. *Annual Review of Earth and Planetary Sciences*, *40*, 226–232. https://doi.org/10.1061/j.epsl.2008.12.006

Sun, N., Stixrude, L., de Koker, N., & Karki, B. B. (2011). First principles molecular dynamics simulations of diopside ($CaMgSi_2O_6$) liquid to high pressure. *Geochimica et Cosmochimica Acta*, *75*(13), 3792–3802. https://doi.org/10.1016/j.gca.2011.04.004

Suzuki, T., Hirata, T., Yokoyama, T. D., & Takahashi, E. (2012). Pressure effect on element partitioning between minerals and silicate melt: Melting experiments on basalt up to 20 GPa. *Physics of the Earth and Planetary Interiors*, *208-209*, 59–73. https://doi.org/10.1016/j.pepi.2012.07.008

Takahashi, E., Shimazaki, T., Tsuzaki, Y., & Yoshida, H. (1993). Melting study of peridotite KLB–1 to 6.5 GPa and the origin of basaltic magmas. *Philosophical transactions of the Royal Society of London Series A*, *342*(1663), 105–120. https://doi.org/10.1098/rsta.1993.0008

Tateno, S., Hirose, K., & Ohishi, Y. (2014). Melting experiments on peridotite to lowermost mantle conditions. *Journal of Geophysical Research: Solid Earth*, *119*, 4684–4694. https://doi.org/10.1002/2013JB010616

Tateno, S., Hirose, K., Sata, N., & Ohishi, Y. (2009). Determination of post-perovskite phase transition boundary up to 4400 K and implications for thermal structure in D″ layer. *Earth and Planetary Science Letters*, *277*(1-2), 130–136. https://doi.org/10.1016/j.epsl.2008.10.004

Tateno, S., Hirose, K., Sinmyo, R., Morard, G., Hirao, N., & Ohishi, Y. (2018). Melting of Fe–Si–S alloys to core pressures: Silicon in the core? *American Mineralogist*, *103*(5), 742–748, https://doi.org/10.2138/am-2018-6299

Tateno, S., Sinmyo, R., Hirose, K., & Nishioka, H. (2009). The advanced ion milling method for preparation of thin film using ion slicer: Application to a sample recovered from diamond-anvil cell. *The Review of Scientific Instruments*, *80*(1), 013901. https://doi.org/10.1063/1.3058760

Taura, H., Yurimoto, H., Kurita, K., & Sueno, S. (1998). Pressure dependence on partition coefficients for trace elements between olivine and the coexisting melts. *Physics and Chemistry of Minerals*, *25*(7), 469–484. https://doi.org/10.1007/s002690050138

Thomas, C. W., Liu, Q., Agee, C. B., Asimow, P. D., & Lange, R. A. (2012). Multi-technique equation of state for Fe_2SiO_4 melt and the density of Fe-bearing silicate melts from 0 to 161 GPa. *Journal of Geophysical Research*, *117*, B10206. https://doi.org/10.1029/2012JB009403

Trønnes, R. G., & Frost, D. J. (2002). Peridotite melting and mineral-melt partitioning of major and minor elements at 22–24.5 GPa. *Earth and Planetary Science Letters*, *197*(1-2), 117–131. https://doi.org/10.1061/S00127–821X(02)004667–1

Walter, M. J., Nakamura, E., Trønnes, R. G., & Frost, D. J. (2004). Experimental constraints on crystallization differentiation in a deep magma ocean. *Geochimica et Cosmochimica Acta*, *68*, 4267–4284. https://doi.org/10.1016/j.gca.2004.03.014

Wang, F. L., Tange, Y., Irifune, T., & Funakoshi, K. (2012). P-V-T equation of state of stishovite up to mid-lower mantle conditions. *Journal of Geophysical Research*, *117*, B06209. https://doi.org/10.1029/2011JB009100

Wang, W., & Takahashi, E. (1999). Subsolidus and melting experiments of a K-rich basaltic composition to 27 GPa: implication for the behavior of potassium in the mantle. *American Mineralogist*, *84*, 357–361. https://doi.org/10.2138/am-1999–0319

Yasuda, A., Fujii, T., & Kurita, K. (1994). Melting phase relations of an anhydrous mid- ocean ridge basalt from 3 to 20 GPa: implications for the behavior of subducted oceanic crust in the mantle. *Journal of Geophysical Research*, *99*, 9401. https://doi.org/10.1029/93JB03205